Macromolecules

ARTICLE

pubs.acs.org/Macromolecules

Microsecond Analysis of Quasi-Smectic Fibrillar Structure in the Continuous Fiber Drawing of Poly(ethylene terephthalate)

Kyoung-Hou Kim,[†] Takahisa Murata,[†] Young-Ah Kang,[‡] Yutaka Ohkoshi,[*,†] Yasuo Gotoh,[†] Masanobu Nagura,[†] and Hiroshi Urakawa[§]

[†]Faculty of Textile Science and Technology, Shinshu University, 3-15-1 Tokida, Ueda, Nagano386-8567, Japan

[‡]Research Institute of Human Ecology, Dong-A University, 840 Hadan2-dong, Saha-gu, Busan 604-714, Republic of Korea

[§]Faculty of Engineering and Design, Kyoto Institute of Technology, Goshokaidou-cho, Matsugasaki, Sakyo-ku, Kyoto 606-8585, Japan

ABSTRACT: Structure devpelopment in the continuous laser-drawing process of poly(ethylene terephthalate) fibers was investigated with a time resolution of 0.2 ms by real time synchrotron X-ray diffraction and fiber temperature measurements. The (001′) and (003′) reflections of a quasi-smectic fibrillar structure were observed from 0.16 ms after necking, and the reflection intensity reached a maximum at around 0.3 ms after necking, when the elastic energy stored at the necking had been released. The *d*-spacing of the (001′) reflection decreased with increasing time, and the quasi-smectic fibrillar structure had a length of 70 nm and a radius of 7.0 nm. The crystallization induction time and crystallization rate were 0.3 ms and 1100 s^{-1} based on the fiber temperature profile and 0.6 ms and 1400 s^{-1} based on the equatorial reflection intensity profiles. In the azimuthal intensity profile under the $2\theta/\theta$ arrangement, a single meridional peak of the (003′) plane was observed, and it is considered that the quasi-smectic fibrillar structure oriented uniaxially along the fiber axis with an orientation factor of 0.986.

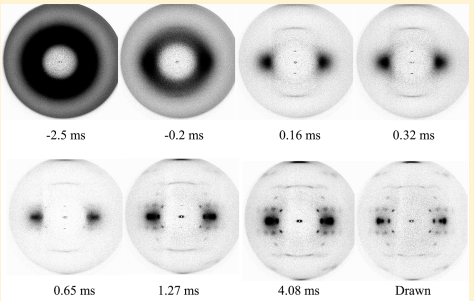

WAXD images taken at various elapsed times after necking. The elapsed times are noted under each image.

1. INTRODUCTION

Poly(ethylene terephthalate) (PET) is the most extensively used polyester and is mainly used in the form of fibers and films. Despite its common use, the relationship between the structure and properties of PET is not fully understood. Many structural models[1−5] have been proposed for semicrystalline polymers, but the ability to predict the resultant properties of such polymers quantitatively on the basis of structure parameters obtained from these models remains insufficient. This is presumably because the structure parameters fail to describe the actual morphology of the molecular chain.

The morphology of the molecular chain of highly oriented PET fibers is mainly decided by the orientation-induced crystallization that occurs during the melt-spinning or drawing process. Kaji et al. have reviewed the spinodal crystallization process from an unstable polymer melt.[6] Several researchers have discussed the mesomorphic structure that arises during the orientation-induced crystallization of PET. This mesophase is induced by stretching an isotropic amorphous structure and exists as a precursor to the crystal. Imai et al.[7] proposed an ordering process during the induction period of PET crystallization before crystal nucleation. Parallel ordering of molecular segment occurs due to an increase in the polymer chain rigidity, and after this ordering proceeds to a certain level, crystallization starts. Kawakami et al.[8] observed a series of strain-induced phase transitions by wide-angle X-ray diffraction (WAXD), including phase transitions from an isotropic slush (a mixture of amorphous and nematic phases) to an oriented slush, from the oriented slush to smectic C, from smectic C to quasi-smectic A, and from quasi-smectic A to a triclinic crystal. However, most studies on the drawing process were conducted under a low deformation speed and a low draw ratio.[9−17] Because the structure development of highly oriented PET is completed in a few milliseconds, it is difficult to measure directly by a batch drawing system. It is also difficult to measure by a continuous drawing system because it is hard to ensure a cross-sectional uniformity in temperature at a high deformation speed and to ensure a well-defined necking position, which fluctuates in the range from several tens to several hundred times the fiber diameter.

Using CO_2 laser drawing, our research group has succeeded in online characterization of the position at which neck deformation occurs. The position can be fixed to within almost 0.2 mm because laser irradiation enables rapid heating of the running fiber without contact. Development of the fiber structure in the vicinity of the necking position has been researched by online characterization using such laser drawing systems.[18−24] In particular, by utilizing the synchrotron X-ray scattering apparatus at SPring-8, we have been able to analyze the structure development of PET, poly(trimethylene terephthalate) (PTT), and poly(ethylene naphthalate) (PEN) fibers.[21−24] For PET and PEN it was revealed that a fibrillar structure having smectic-like, two-dimensional ordering was developed prior to orientation-induced crystallization. This interpretation was based on the fact that a meridional (001′) reflection was observed immediately after neck deformation, which disappeared after a few milliseconds.

Received: June 1, 2011
Revised: August 6, 2011
Published: August 31, 2011

The fibrillar structure supports the entire body of the fiber under an external stress and is very important in determining its mechanical properties.

Moreover, because of the triclinic system of the PET crystal, the molecular chains in the PET crystal were inclined against the deformation direction, a process called "tilting". Bunn[25] has reported that the *c*-axis was tilted by about 5° with the (−230) plane against the deformation direction. However, because there has been little study on the initial stages of the fiber structure development, it is not clear whether the quasi-smectic fibrillar structure was tilted or not.

In this study, the structure development of highly oriented PET fibers in a continuous laser drawing process was analyzed with much higher time resolution than studies reported to date. In particular, we have been able to focus on the structural changes occurring in transition from a quasi-smectic fibrillar structure to a fiber structure, which largely occur within 1 ms of necking. By increasing the fiber running speed, we attained a time resolution of 0.2 ms. We have also analyzed the size and orientation of the quasi-smectic fibrillar structure. For this purpose, we acquired WAXD images under a $2\theta/\theta$ arrangement to elucidate the *d*-spacing, size, and orientation of the third-layer diffraction of the quasi-smectic fibrillar structure.

2. EXPERIMENTAL SECTION

Materials and Drawing Conditions. PET pellets, provided by Toyobo Co. Japan, were melt-spun with a mass flow rate of 5.0 g/min and a take-up speed of 212 m/min. The fiber produced was 155 ± 3 μm in diameter and exhibited an amorphous halo in the WAXD image and a birefringence of 1.0×10^{-3}, which indicates that the obtained fiber was almost entirely unoriented and amorphous. The PET fiber was drawn up to 5.5 times with a take-up speed of 121 m/min. The applied laser power as measured with a power meter (Synrad Co. Ltd., PW-250) was 25−27 W, and the drawing stress as determined using a tension meter was 120−130 MPa.

Fundamentals of Online Measurement. The online measurement system used in this study is schematized in Figure 1. Details of the online system can be found in previous papers.[18−24] As described in detail elsewhere, the running fiber was heated by means of a CO_2 laser beam which was generated using a PIN-30S laser source (Onizuka Co., Ltd.). The laser source had a rated power of 30 ± 1 W and a laser beam diameter of 6 mm. The fiber was drawn by the speed difference between the feed and take-up rollers. Fixing of the necking position by laser irradiation allows for highly stable and well-established steady states to be monitored in the continuous neck-drawing process. The WAXD image and the fiber temperature were measured as a function of elapsed time *t*, which was calculated on the basis of the distance (D) between the measurement point and the necking point divided by the fiber running speed (v). The distance D can be changed by shifting the necking position with a traveling mirror unit. Monitoring of the neck-drawing position by a CCD video camera image was also performed, with a length of 4.7 mm corresponding to 640 pixels.

Fiber Temperature Measurement. Temperature of the running fiber on the drawing process was measured using an infrared thermometer (TMZ7N2-J0-5K1-2, Japan Sensor Co., Ltd.). An HgCdTe detector with a response time of 10 ms was used. The thermometer was equipped with an interference filter of 5.78 μm in wavelength, which corresponds to the stretching mode of the PET carbonyl group. Further details on the online fiber temperature measurements can be found in previous reports.[18−20]

X-ray Diffraction Measurement. The synchrotron radiation X-ray source of the Beamline 40B2 at SPring-8 was used in this study.

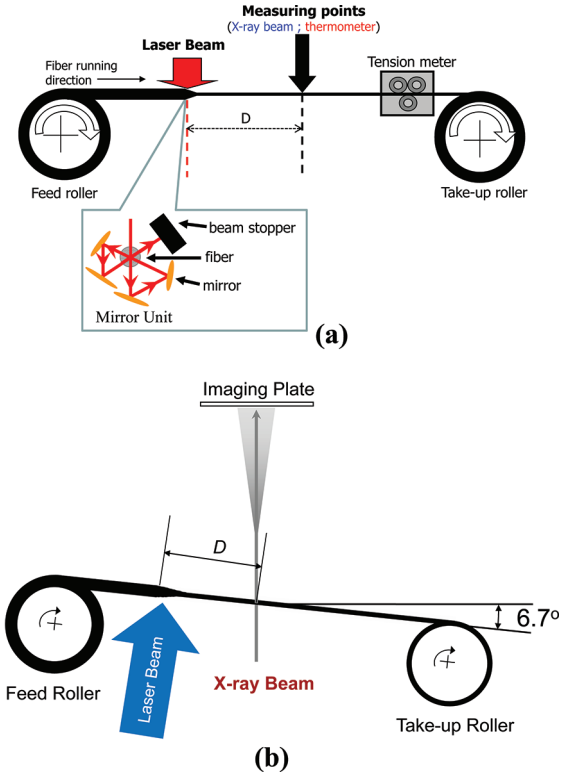

Figure 1. Schematic diagram of online measurement system (a). Setup for inclined X-ray diffraction measurements (b).

The wavelength of the X-ray beam was 0.071 nm, and the beam had an ellipse shape of 120 μm in the vertical axis and 340 μm in the horizontal axis. WAXD images were taken by a 3000 × 3000 pixel imaging plate with a 400 mm vacuum chamber for an exposure time of 360 s. The sample-to-detector distance was 420.8 ± 1.0 mm, which was calibrated by the diffraction patterns of lead stearate (StPb), lead dioxide (PbO_2), and hexamethylenetetramine ($C_6H_{12}N_4$). The necking position was determined from the transmitted X-ray intensity profile obtained from an ion chamber. The peaks corresponding to the polyimide film mounted on the vacuum chamber and background scattering were compensated by subtracting a blank image.

As seen in Figure 1b, inclined X-ray diffraction patterns were also acquired. To obtain an inclined WAXD pattern under a $2\theta/\theta$ arrangement for the (003′) reflection of the PET mesophase, an inclined angle of 6.7° was selected because the (003′) reflection appears at $2\theta = 13.36°$ when the X-ray wavelength is 0.08 nm.

The time resolution was calculated by dividing the position resolution ($W_{X\text{-ray}}$) by the fiber running speed (v). The position resolution was calculated by eq 1 based on the diameter of the X-ray beam (W_{beam}: 340 μm), the length of the necking region (W_{neck}: 75 μm), and fluctuations in the necking point (W_{deform}: 112−289 μm). Both the average position and fluctuations in the necking point were calculated from the necking points observed by image analysis of the recorded CCD video images taken during measurement. As a result, the time resolution was found to be 0.18−0.23 ms for the present study.

$$W_{X\text{-ray}} = \sqrt{{W_{beam}}^2 + {W_{neck}}^2 + {W_{deform}}^2} \quad (1)$$

3. RESULTS AND DISCUSSION

Fiber Temperature. The fiber temperature profile during the laser drawing is shown in Figure 2. The origin of the horizontal

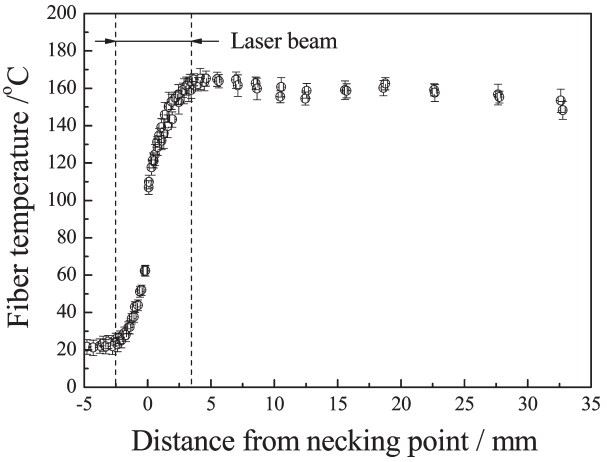

Figure 2. Fiber temperature profile as a function of distance from the necking point during laser drawing.

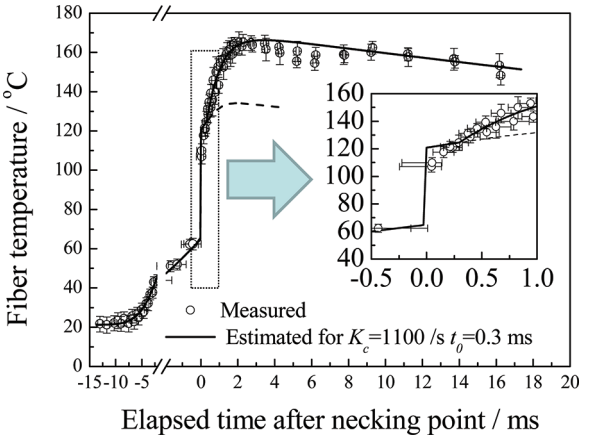

Figure 3. Measured and estimated fiber temperatures. Fiber temperatures were estimated by eq 2 with (—) or without (---) consideration of the latent heat of crystallization as given in eq 3.

axis denotes the position where the necking occurred. The laser beam has a diameter of 6 mm, as shown by the broken lines, and its center was positioned at 0.46 mm after the necking point. The fiber temperature was measured twice, with both values shown in the figure. The fiber temperature began to rise upon irradiation by the laser beam and increased steeply at the necking point. With this steep increase, the fiber temperature moved across the glass transition temperature (T_g) of PET. Ultimately, the fiber temperature attained a maximum of about 165 °C at the end point of laser irradiation, before cooling gradually by the ambient air.

The fiber temperature profile can be simulated by the following energy balance equation:[21]

$$\Delta T = \frac{1}{wC_p}\{I(x)D_fA(D_f)\Delta x - \pi D_f h(T - T_a) + F\Delta v\} + \frac{\Delta H_c}{C_p}\Delta\chi \quad (2)$$

where w, C_p, and D_f are the mass flow rate, specific heat, and fiber diameter, respectively. The first term, which denotes heating by the CO_2 laser irradiation, was calculated based on the intensity profile of the laser beam $I(x)$ and the absorbance A of the CO_2 laser light for PET. The second term, which represents the cooling by air, is a function of the fiber temperature T, ambient temperature T_a, and heat transfer coefficient h, in which the heat transfer coefficient is calculated using the formula reported by Kase et al.[26] The third term, indicating the exothermic heat of plastic deformation, was calculated from the drawing force F and fiber velocity v, assuming that all the applied work was immediately converted to thermal energy at the necking point. The fourth term, which expresses the exothermic heat of crystallization, was calculated based on the heat of fusion for the perfect crystal ΔH_c[27] and the degree of crystallinity χ. The crystallization was assumed to start at the necking point, and the degree of crystallinity χ was calculated by an Avrami-like equation (eq 3), with the crystallization induction time t_0 after necking obtained assuming one-dimensional heterogeneous nucleation, where K is the crystallization rate, t is the elapsed time after necking, X is the degree of crystallization at time t, and X_∞ is that of the drawn fiber.

$$X(t) = X_\infty[1 - \exp\{-K(t - t_0)\}] \quad (3)$$

Figure 3 shows the measured and simulated fiber temperature profiles with elapsed time after necking. The fiber temperature profiles were simulated for two conditions: one assuming K_c = 1100 s^{-1} and t_0 = 0.3 ms (solid line) and the other ignoring the exothermic heat of crystallization (broken line). The solid line corresponded well to the measured temperature, whereas the broken line did not match the measured data after necking. The solid line deviates from the measured data immediately after necking but corresponds well in the region from 0.3 to 3.5 ms after necking. The deviation just after necking may be attributed to partial storage of the plastic deformation energy, i.e., the work of external force applied at the necking, as potential energy,[19,20] and the close correspondence after the elapsed time of 0.3 ms may indicate that the stored potential energy had been released during the induction time.

As mentioned in the following section, the amount of quasi-smectic fibrillar structure[21] takes a maximum at about 0.3 ms, which strongly suggests that the stored potential energy promotes the development of a quasi-smectic structure.

X-ray Diffraction Patterns. WAXD patterns taken on the laser drawing line are shown in Figure 4. The pattern taken at the negative elapsed time of −2.5 ms, representing the time before necking (i.e., the undrawn fiber), shows an amorphous halo. The halo became concentrated along the equatorial axis at −0.2 ms, at the pattern was seen to be overlapped by those of the drawn and undrawn fibers, considering the time resolution of about 0.2 ms. At 0.16 ms, streaklike reflections appeared along the meridian, corresponding to the (001′) and (003′) reflections of the quasi-smectic structure. Because the reflections had a streaklike shape, the quasi-smectic structure should have a fibrillar shape along the fiber axis.[21] The intensities of (001′) and (003′) reflections reached a maximum at 0.32 ms and gradually decreased with the appearance of crystal reflections, which suggests that the quasi-smectic fibrillar structure transformed into a triclinic crystal of PET in the process of orientation-induced crystallization.

Intensity profiles obtained from the patterns are shown in Figure 5. The profiles were calculated with an integral width of 10 pixels using the R-axis software created by Rigaku Co. The integrated intensity of each reflection can be considered to be almost proportional to the relative fractions of the quasi-smectic mesophase and the triclinic crystal phase because of the high degree of orientation of the reflections and minimal fluctuations in the X-ray irradiating volume. The latter condition for the X-ray

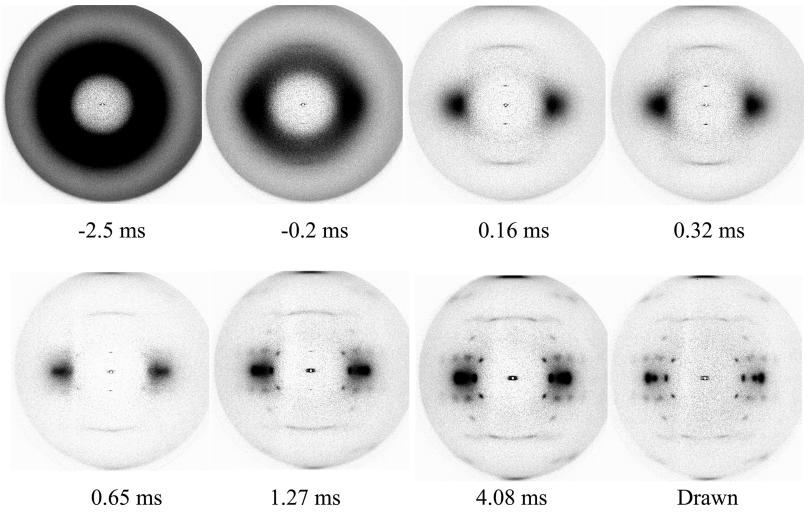

Figure 4. WAXD images taken at various elapsed times after necking. The elapsed times are noted under each image.

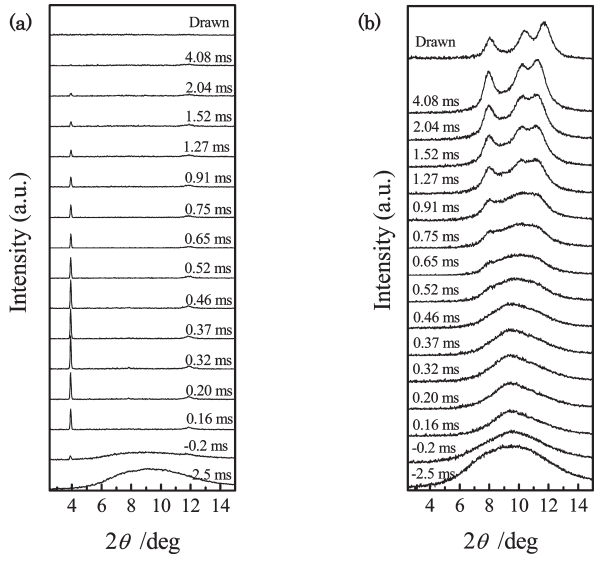

Figure 5. WAXD intensity profiles along the meridional (a) and equatorial (b) directions. Elapsed times after necking are noted in the figures.

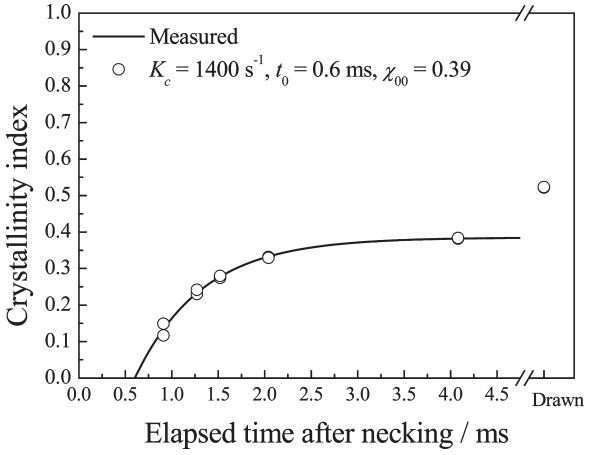

Figure 6. Crystallinity index obtained from equatorial X-ray diffraction intensity profiles. The crystallization rate calculated by the Avrami equation is noted in the figure.

beam can be expected to be less than 289 μm in the vertical direction and 340 μm in the horizontal direction.

The (001′) reflection near $2\theta = 4°$, which emerged at −0.2 ms, increased to its maximum intensity at 0.32−0.46 ms, then decreased with increasing time, and nearly disappeared at 4.08 ms. The decrease in the (001′) reflection in the range of 0.52−2.04 ms corresponded to the appearance and development of crystal reflection. Accordingly, it is considered that the (001′) reflection represents the quasi-smectic fibrillar structure, which decreases when crystal reflection appears and disappears entirely upon complete adoption of the crystal structure. In the drawn fiber, clear crystal reflection peaks were observed and were found at higher angles than those obtained by online measurements. This was due to an increase in the density of the unit cell caused by thermal shrinkage.[21]

The meridional (001′) and (003′) reflections obtained at various elapsed times were fitted by a Gaussian function with a linear background. The intensities and widths of the peaks were used for the following analysis. The intensity profile of the (001′) reflection along the equatorial direction was also fitted by a Gaussian function, and the radius of gyration of the quasi-smectic fibrillar structure was estimated by a Guinier equation assuming a cylindrical scattering body. For intensity profiles from −0.2 to 2.04 ms, the fitting curves were well fitted to the measured profiles.

Amount of Crystallinity. Figure 6 shows the crystallinity index obtained from the equatorial X-ray diffraction intensity profile (see Figure 5b). The crystallinity index is defined as the ratio of the integral intensity of the (010), (−110), and (110) crystal reflections to the total integral intensity from $2\theta = 3°$ to 15°. The crystallinity index was also fitted by the Avrami-like formula given by eq 3, which gave $K_c = 1400\ s^{-1}$, $x_\infty = 0.39$, and $t_0 = 0.6$ ms as a result. Because the K_c and t_0 values are similar to those based on the fiber temperature profile, it is considered that the potential energy was largely released upon crystal formation.

Amount of Quasi-Smectic Structure. Figure 7 shows the integrated intensities of the fitted (001′) and (003′) reflection peaks. Although the position resolution, $W_{X\text{-ray}}$ (see eq 1), was

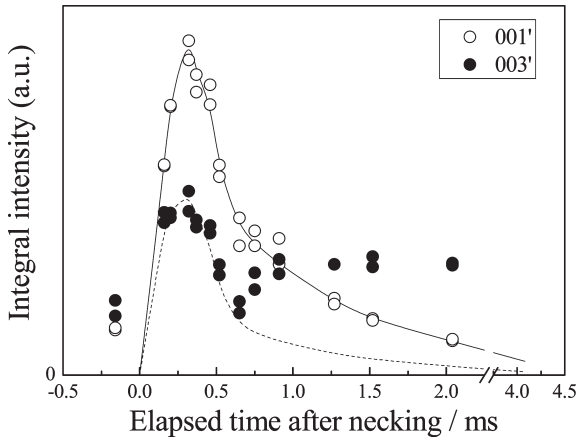

Figure 7. Integrated intensity of the (001′) and the (003′) diffractions over time. The (003′) data likely has a contribution from the (−103) crystal diffraction.

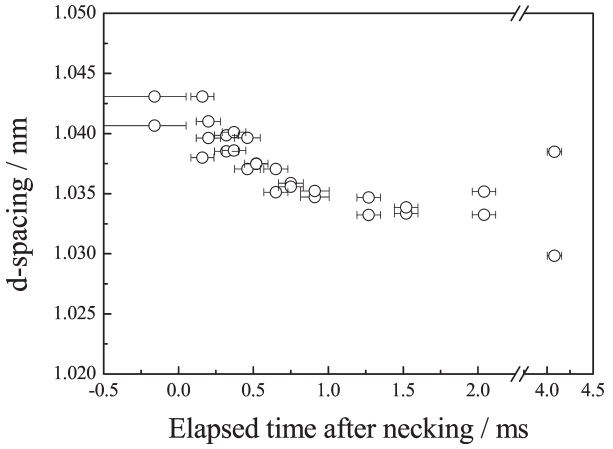

Figure 8. Change in *d*-spacing of the (001′) diffraction over time.

almost constant, the time resolution changed due to the difference in fiber running speed before and after necking. Therefore, the values obtained from the reflection pattern at -0.2 ± 1.0 ms have considerable uncertainty due to overlapping of the patterns before and after necking, whereas the reflection pattern of $+0.16 \pm 0.18$ ms is regarded as the pattern mainly after necking. Thus, the integrated intensity of the (001′) and (003′) reflection peaks at −0.2 ms is believed to have a contribution from the pattern after necking.

The integrated intensities of the (001′) and (003′) reflections varied similarly over time until 0.6 ms. That is, both intensities increased sharply after necking, reaching a maximum at 0.32 ms after necking, and then decreased gradually. In the previous section, we obtained a crystallization induction time of $t_0 = 0.3$ ms based on the fiber temperature and a time of $t_0 = 0.6$ ms based on the integrated reflection intensity. At 0.3 ms after necking, the (001′) and (003′) integrated intensities reached a maximum, indicating that the potential energy stored at necking had been released. The stored energy is known to be a factor in strongly promoting the development of the quasi-smectic structure. The integrated intensity of the (003′) reflection increased after about 0.6 ms, but this may be a result of overlap by the (−103) reflection.

***d*-Spacing of Quasi-Smectic Structure.** Figure 8 shows the *d*-spacing of the (001′) reflection over time. The *d*-spacing was calculated by Bragg's equation with 2θ obtained by Gaussian fitting of the curves in Figure 5. The *d*-spacing immediately after necking was higher than 1.040 nm, before decreasing gradually to 1 ms, and then saturating at about 1.033 nm. The *d*-spacing of 1.040 nm at 0.16 ms was 3% shorter than the *c*-axis length of PET, which is 1.075 nm,[25] and rather close to the value of 1.03 nm reported by Ran et al.[16] They proposed a smectic C structure in which the molecular axis was inclined at 15.7° against the fiber axis. The inclined angle calculated for the obtained *d*-spacing immediately after necking was 14.7°, which indicates that the quasi-smectic structure corresponds well to the smectic C structure.

Attribution of Third-Layer Reflection. In a previous study,[21] we suggested that the meridional reflections were the (001′) and (003′) reflections of a quasi-smectic fibrillar structure. But it is open to argument whether the third-layer peak is in fact the (003′) reflection. First, their *d*-spacing values did not agree with each other, and second the reflection peak was too broad. These disparities were considered to be a result of the limitations of the $2\theta/0$ arrangement. Therefore, in the present study, to confirm the third-layer peak was the (003′) reflection, the peak position and width along the meridional direction were measured for 0.5 ms under the $2\theta/\theta$ arrangement.

The obtained *d*-spacing of the third-order peak was 0.348 nm, which is about one-third of the *d*-spacing of the (001′) plane (as shown in Figure 8) and is consistent with the (003′) reflection. The proportional manner observed in Figure 7 also suggests that both diffractions are assigned to the same structure—the quasi-smectic structure. The issue of peak width was also resolved as shown in the following analysis.

A Hosemann plot[28] has been commonly used to analyze the crystallite size (L) and the disordering parameter (g_{II}) along the normal direction of the reflection planes. By assuming a Gaussian distribution for the peaks, the above parameters can be estimated using eq 4 based on the half-width (δ) and reflection angle (θ) of a series of lattice planes in the same direction.

$$\left(\frac{\delta_m \cos\theta_m}{\lambda}\right)^2 = \frac{1}{L^2} + \frac{(\pi g_{II} m)^4}{d^4} \quad (4)$$

Figure 9 shows Hosemann plots for the (001′), (002′), and the third-layer peak, i.e., m = 1, 2, and 3 for the (001′) plane. To obtain a linear regression, the peak widths (circles) obtained in the previous study[21] are shown together with the third-layer peak width (triangles) under the $2\theta/\theta$ arrangement. The peak widths obtained under the $2\theta/0$ arrangement were fitted by a regression line to a negative intercept. However, by applying the third-layer peak width under the $2\theta/\theta$ arrangement, a regression line with a positive intercept was obtained. Thus, it is considered that the meridional third-layer peak corresponded to the (003′) reflection of the quasi-smectic fibrillar structure. The obtained L and g_{II} values are 57 nm and 0.02, respectively. These results indicate that the quasi-smectic fibrillar structure has good regularity and a length of about 57 nm along the fiber axis.

Orientation of Quasi-Smectic Fibrillar Structure. To discuss the orientation of the fibrillar structure, the azimuthal intensity profiles of the third-layer reflections obtained under the $2\theta/\theta$ arrangement at $2\theta = 13.3°$ are shown in Figure 10. The (003′) intensity of the quasi-smectic structure was observed as a single meridional peak from 0.25 to 1.0 ms, which disappeared at 4 ms. The (−103) crystal reflection appeared at 1 ms and remained thereafter. The existence of the meridional single peak

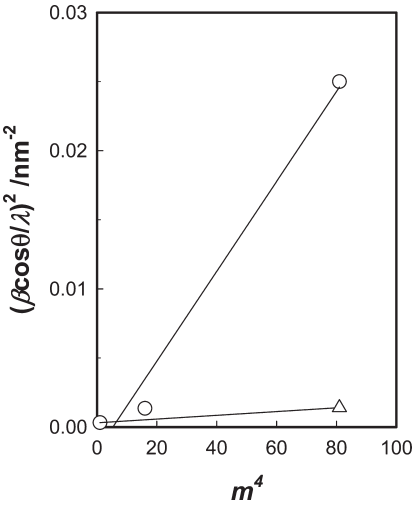

Figure 9. Hosemann plot for meridional (001′), (002′), and (003′) diffractions at 0.5 ms after necking. The peak width β is obtained for tilting angles of 0° (○)[21] and 6.7° (△).

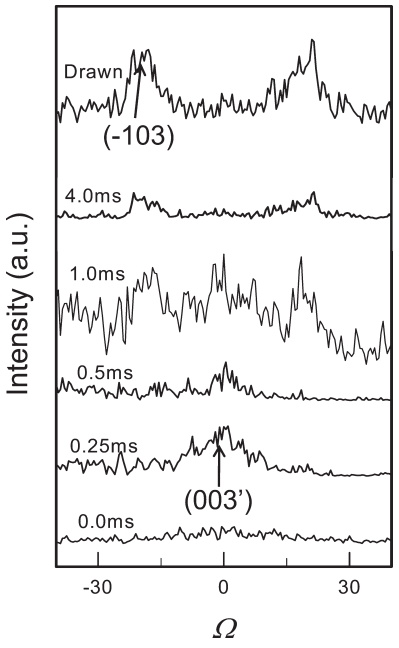

Figure 10. Intensity profiles along the azimuthal angle (Ω) for various elapsed times. The $\theta-2\theta$ arrangement was selected, in which the diffraction angle of 13.3° was fixed with the rotation axis tilted 6.7° from the X-ray beam. Mesophase (003′) and crystal (−103) diffractions are observed.

of the (003′) plane suggests that the smectic fibrillar structure was oriented uniaxially along the fiber axis, as with the (001′) and (002′) reflections.[21]

For a more quantitative analysis, the orientation factor was estimated from the equatorial profiles of the (001′) and (003′) reflections. The meridional peak broadened toward the azimuthal or equatorial direction not only because of disorientation of the fibrillar structure but also because of the limited fibril diameter. To analyze these contributions, we obtained the intensity profiles of the (001′) and (003′) reflections along the equatorial direction and obtained their half-widths (β_{001}, β_{003}) assuming a Gaussian distribution. By assuming a Gaussian distribution, the half-width can be described by the sum of two contributions, the disorientation and the fibril size, as shown in eq 5.

$$\beta_{00l}{}^2 = \beta_D{}^2 + l^2\beta_0{}^2 \quad (5)$$

Here, β_D is the fibril size contribution, l is the order of the reflection, and β_0 is the disorientation contribution. By substituting β_{001} and β_{003} into eq 5, β_0 and β_D values of 0.64° and 0.25° are obtained. The radius of gyration, 7.0 nm, was calculated from β_D, with the assumption that the fibril has a rodlike shape. An orientation factor of the fibril of 0.986 was also calculated from the broadness along the azimuthal direction that is converted from β_0. The obtained fibril orientation factor is almost the same as the crystal orientation factor of about 0.99 reported in our previous study.[21] This indicates that the orientation of the quasi-smectic precursor determines the orientation of the resultant crystallites.

4. CONCLUSION

The structure development in the continuous laser-drawing process of PET fibers was analyzed with the time resolution of ~0.2 ms by real-time X-ray diffraction and fiber temperature measurements. Within 1 ms after necking, the structural transition occurred from the quasi-smectic fibrillar structure to the fiber structure. The (001′) and (003′) reflections of a quasi-semectic fibrillar structure were observed at 0.16 ms after necking, and the reflection intensity reached a maximum at around 0.3 ms after necking, when the elastic energy stored at the necking had been released. The reflection intensities decreased with the appearance of crystalline reflections, which suggested that the quasi-smectic fibrillar structure transformed into the PET crystal through the orientation-induced crystallization. The quasi-smectic fibrillar structure was 70 nm in length and 7.0 nm in radius, with the assumption that the fibril has a rodlike shape. The crystallization induction time and crystallization rate were 0.3 ms and 1100 s^{-1} based on the fiber temperature profile and 0.6 ms and 1400 s^{-1} based on the equatorial diffraction intensity profiles. In the azimuthal intensity profile under the $2\theta/\theta$ arrangement, a single meridional peak of the (003′) plane was observed from 0.25 to 1.0 ms, and it is considered that the quasi-smectic fibrillar structure oriented uniaxially along the fiber axis with an orientation factor of 0.986.

■ ACKNOWLEDGMENT

The synchrotron radiation experiments were performed at the BL40B2 SPring-8 with the approval of the Japan Synchrotron Radiation Research Institute (JASRI) (Proposal Nos. 2006B1396, 2007A1674, and 2008A1485). This research was supported by Grant-in-Aid No. 18550191 from the Japan Society for the Promotion of Science. This work was also supported by the "Innovation Creative Center for Advanced Interdisciplinary Research Areas (Shinshu University)", a project to specially coordinate funds for promoting Science and Technology by the Ministry of Education, Culture, Sports, Science and Technology of the Japanese government.

■ REFERENCES

(1) Peterlin, A.; Ingram, P.; Kiho, H. *Makromol. Chem.* **1965**, *86*, 294.
(2) Zaukelies, D. A. *J. Appl. Phys.* **1962**, *33*, 3235.

(3) Beresford, D. R.; Bevan, H. *Polymer* **1964**, *5*, 247.
(4) Dismore, F.; Statton, W. O. *J. Polym. Sci.* **1966**, *C13*, 133.
(5) Somani, R. H.; Yang, L.; Zhu, L.; Hsiao, B. S. *Polymer* **2005**, *46*, 8587.
(6) Kaji, K.; Nishida, K.; Kanaya, T.; Matsuba, G.; Konishi, T.; Imai, M. *Adv. Polym. Sci.* **2005**, *191*, 187.
(7) Imai, M.; Kaji, K.; Kanaya, T.; Sakai, Y. *Phys. Rev. B* **1995**, *52* (17), 12696.
(8) Kawakami, D.; Hsiao, B. S.; Burger, C.; Ran, S.; Avila-Orta, C.; Sics, I.; Kikutani, T.; Chu, B. *Macromolecules* **2005**, *38*, 91.
(9) Fujimoto, K.; Iohara, K.; Owaki, S.; Murase, Y. *Sen'i Gakkaishi* **1988**, *44*, 53.
(10) Kikutani, T.; Kawahara, Y.; Matsui, T.; Takaku, A.; Shimizu, J. *Seikei-Kakou* **1989**, *1*, 333.
(11) Schultz, J. M.; Hsiao, B. S.; Samon, J. M. *Polymer* **2000**, *41*, 8887.
(12) Mahendrasingam, A.; Marian, C.; Fuller, W.; Blundell, D. J.; Oldman, R. J.; Harvie, J. L.; Mackerron, D. H.; Riekel, C.; Engstrom, P. *Polymer* **1999**, *40*, 5553.
(13) Blundell, D. J.; Mahendrasingam, A.; Marian, C.; Fuller, W.; Mackerron, D. H.; Harvie, J. L.; Oldman, R. J.; Riekel, C. *Polymer* **2000**, *41*, 7793.
(14) Welsh, G. E.; Blundell, D. J.; Windle, A. H. *Macromolecules* **1998**, *31*, 7562.
(15) Kawakami, D.; Ran, S.; Burger, C.; Fu, B.; Sics, I.; Chu, B.; Hsiao, B. S. *Macromolecules* **2003**, *36*, 9275.
(16) Ran, S.; Zong, X.; Fang, D.; Hsiao, B. S.; Chu, B.; Ross, R. *J. Appl. Crystallogr.* **2000**, *33*, 1031.
(17) Fukao, K.; Koyama, A.; Tahara, D.; Kozono, Y.; Miyamoto, Y.; Tsurutani, N. *J. Macromol. Sci., Phys.* **2003**, *42B*, 717.
(18) Okumura, W.; Yamaguchi, T.; Ohkoshi, Y.; Gotoh, Y.; Nagura, M. *Int. Polym. Proc.* **2002**, *17*, 125.
(19) Yamaguchi, T.; Ohkoshi, Y.; Gotoh, Y.; Nagura, M. *Seikei-Kakou* **2005**, *17*, 649.
(20) Yamaguchi, T.; Komoriyama, K.; Ohkoshi, Y.; Urakawa, H.; Gotoh, Y.; Terasawa, N.; Nagura, M.; Kajiwara, K. *J. Polym. Sci., Part B: Polym. Phys.* **2005**, *43*, 1090.
(21) Yamaguchi, T.; Kim, K. H.; Murata, T.; Koide, M.; Hitoosa, S.; Urakawa, H.; Ohkoshi, Y.; Gotoh., Y.; Nagura, M.; Kodera, M.; Kajiwara, K. *J. Polym. Sci., Part B: Polym. Phys.* **2008**, *46*, 2126.
(22) Kim, K. H.; Yamaguchi, T.; Ohkoshi, Y.; Gotoh, Y.; Nagura, M.; Urakawa, H.; Kodera, M.; Kikutani, T. *J. Polym. Sci., Part B: Polym. Phys.* **2009**, *47* (17), 1653.
(23) Kim, K. H.; Kang, Y. A.; Murata, T.; Ikehata, S.; Ohkoshi, Y.; Gotoh, Y.; Nagura, M.; Koide, M.; Urakawa, H.; Kotera, M. *Polymer* **2008**, *49*, 5705.
(24) Kim, K. H.; Aida, R.; Kang, Y. A.; Ohkoshi, Y.; Gotoh, Y.; Nagura, M.; Urakawa, H. *Polymer* **2009**, *50* (19), 4429.
(25) Daubeny, R. P.; Bunn, C. W.; Brown, C. J. *Proc. R. Soc. London, Ser. A* **1954**, *226*, 531.
(26) Kase, S.; Matsuo, T. *J. Polym. Sci., Part A: Polym. Chem.* **1965**, *3*, 2541.
(27) Gaur, U.; Mehta, A.; Wunderlich, B. *J. Therm. Anal.* **1978**, *13* (1), 71.
(28) Bonart, R.; Hosemann, R.; McCullough, R. L. *Polymer* **1963**, *4*, 199.